

Three-dimensional modeling of alternating current triboelectric nanogenerator in the linear sliding mode

Jiajia Shao^{1,2}, Di Liu^{1,2}, Morten Willatzen^{1,2,a)}, and Zhong Lin Wang^{1,2,3,a)}

¹CAS Center for Excellence in Nanoscience, Beijing Key Laboratory of Micro-nano Energy and Sensor, Beijing Institute of Nanoenergy and Nanosystems, Chinese Academy of Sciences, Beijing 100083, China

²College of Nanoscience and Technology, University of Chinese Academy of Sciences, Beijing 100049, People's Republic of China

³School of Materials Science and Engineering, Georgia Institute of Technology, Atlanta, Georgia 30332-0245, United States

^{a)}Authors to whom correspondence should be addressed: mortenwillatzen@binn.cas.cn and zhong.wang@mse.gatech.edu

ABSTRACT

Energy harvesting from mechanical motions has immense applications such as self-powered sensors and renewable energy sources powered by ocean waves. In this context, the triboelectric nanogenerator is the cutting-edge technology which can effectively convert ambient mechanical energy into electricity through the Maxwell's displacement current. While further improvements of the energy conversion efficiency of triboelectric nanogenerators critically depend on theoretical modeling of the energy conversion process, to date only models based on single-relative-motion processes have been explored. Here, we analyze energy harvesting of triboelectric nanogenerators using a three-dimensional model in a linear-sliding mode and demonstrate a design of triboelectric nanogenerators that have a 77.5% enhancement in the average power in comparison with previous approaches. Moreover, our model shows the existence of a DC-like bias voltage contained in the basic AC output from the energy conversion, which makes the triboelectric nanogenerators an energy source more pliable than the traditional AC power generation systems. The present work provides a framework for systematic modeling

of triboelectric nanogenerators and reveals the importance of obtaining direct analytical insight in understanding the current output characteristics of the triboelectric nanogenerators. Incorporating our model analysis in future designs of triboelectric nanogenerators is beneficial for increasing the energy conversion power and may provide insights that can be used in engineering the profile of the output current of the nanogenerators.

Keywords: triboelectric nanogenerator, alternating current output, displacement current, three-dimensional model, effective values

1. INTRODUCTION

The United Nations' climate goal is to limit the average global temperature rise caused by greenhouse gas emissions to below 2°C compared with pre-industrial levels.^{1,2} However, several studies indicate that the unabated use of all current fossil fuel reserves is incompatible with this target.^{3,4} For instance, coal still accounted for 28% of the global energy supply despite the global efforts have shifted from non-renewable to renewable energy forms.⁵ Implementation of renewable energy technologies such as natural gas, wind or solar is an essential part of the strategy.^{5,6} Recently, a new and effective mechanical energy harvesting technology, the triboelectric nanogenerator (TENG), has been developed. A TENG can directly convert mechanical triggering energy into electricity by producing alternating current (AC). Given the universal and ubiquitous access to triboelectrification, TENGs have a high promising potential as the energy source to power randomly distributed electronic devices and multifunctional array of sensing systems. It has been demonstrated that TENGs can be used in four major application fields: self-powered sensors, direct high-voltage power sources, micro/nano power sources and large-scale blue energy.^{7,8}

The fundamental principle of a TENG is based on the Maxwell's displacement current (I_D). The displacement current is generated in TENGs due to vertical or horizontal movement of the contacting materials with opposite electrostatic charges. Although we know that the displacement current is equal to the conduction current in the external circuit of TENGs, the quantitative details and insight on how the variation of the three-dimensional (3D) spatially-distributed electric displacement affects the generation of the displacement current, for different TENG mode geometries, have not yet been addressed.⁹ To date, a large number of theoretical works have been published with the aim of qualitatively explaining either the working principles or describing its output behavior.¹⁰⁻²⁶

However, AC outputs of different modes of TENGs have not been investigated systematically despite the significant importance for practical applications.^{27,28} Hitherto, research on TENG characteristics and dynamics has mainly focused on one single relative motion process while very little research work has been carried out on the AC output of TENG's subject to periodic mechanical motion.^{9,19,29}

Here, we analyze the generation of displacement current using a simple 3D mathematical model for a linear-sliding mode TENG. Firstly, our results suggest that periodic variations of the electric field lead to, after relaxation, the generation of a periodic variation of I_D of opposite phase. It is shown that a similar direct current (DC) bias is contained in the AC output signal that is a characteristic of TENGs entirely different from conversional power generation methods. Utilizing the optimum value of the capacitance resistance for steady state operation, a substantial increase (77.5% improvement) is obtained for the power generation in comparison with the traditional strategy reported for relaxation-time studies. We derive analytical equations of relaxation and cycle times as well as the optimum resistance in steady state. Based on a dimensional analysis, we present a normalized governing equation of TENGs and use it to obtain an expression for the structural figure-of-merit. We anticipate that, the analytical strategy presented here for the slide-mode TENG is transferable to other types of TENGs.

2. 3D MATHEMATICAL MODEL OF THE LINEAR SLIDING MODE TENG

2.1 Output performance at open-circuit (OC) condition

A 3 dimensional model that we have established before can be utilized to evaluate the output performance of the linear sliding (LS) mode TENG. Consider the geometry in Fig. 1(a). The upper bar slides back and forth on the lower bar and triboelectric charges are generated dynamically on the surface parts that don't overlap. At the OC condition, the electric field can be found (Supplementary Note 1):

$$\begin{aligned}
 E(x, y, z, t) = & -\frac{\sigma_T}{4\pi\epsilon(\mathbf{r})} \int_0^{a(t)} dx' \int_{-b/2}^{b/2} \frac{(x-x', y-y', z-z_{0^-})}{((x-x')^2 + (y-y')^2 + (z-z_{0^-})^2)^{3/2}} dy' \\
 & + \frac{\sigma_T}{4\pi\epsilon(\mathbf{r})} \int_L^{L+a(t)} dx' \int_{-b/2}^{b/2} \frac{(x-x', y-y', z-z_{0^+})}{((x-x')^2 + (y-y')^2 + (z-z_{0^+})^2)^{3/2}} dy' \\
 & + \frac{\sigma_T}{4\pi\epsilon(\mathbf{r})} \int_0^{a(t)} dx' \int_{-b/2}^{b/2} \frac{(x-x', y-y', z-z_1)}{((x-x')^2 + (y-y')^2 + (z-z_1)^2)^{3/2}} dy' \\
 & - \frac{\sigma_T}{4\pi\epsilon(\mathbf{r})} \int_L^{L+a(t)} dx' \int_{-b/2}^{b/2} \frac{(x-x', y-y', z-z_2)}{((x-x')^2 + (y-y')^2 + (z-z_2)^2)^{3/2}} dy' \\
 & + \frac{\sigma_E}{4\pi\epsilon(\mathbf{r})} \int_{a(t)}^L dx' \int_{-b/2}^{b/2} \frac{(x-x', y-y', z-z_1)}{((x-x')^2 + (y-y')^2 + (z-z_1)^2)^{3/2}} dy' \\
 & - \frac{\sigma_E}{4\pi\epsilon(\mathbf{r})} \int_{a(t)}^L dx' \int_{-b/2}^{b/2} \frac{(x-x', y-y', z-z_2)}{((x-x')^2 + (y-y')^2 + (z-z_2)^2)^{3/2}} dy'
 \end{aligned} \tag{1}$$

where $a(t)$ represents the relative motion distance and L is the length of the electrode/dielectric. On the overlapping parts of the electrode. i.e., when x is between $a(t)$ and L , a charge density exists equal in magnitude but of opposite sign to the triboelectric charge density of the dielectric material in direct contact with the electrode. For the overlapping part of the bottom (top) electrode a different charge density $\sigma_E(t)$ ($-\sigma_E(t)$) exists at any time. In addition, we have introduced the notation z_{0^-} to indicate that negative triboelectric charges are generated at a z value infinitesimally smaller than z_0 . Similarly, z_{0^+} indicates that positive triboelectric charges are generated at a z value infinitesimally larger than z_0 . With this method, we have calculated the electric potential and potential difference between the two electrodes (Supplementary Note 1). This is also crucial when we next evaluate the displacement current.

For OC conditions the charge density $\sigma_E(t)$ is determined by the requirement that the total charge σ_0 on the electrodes must be zero at any time (Supplementary Note 2). According to the definition, the displacement current through the internal TENG surface z at OC conditions ($I_{D,OC}$) is

This is the author's peer reviewed, accepted manuscript. However, the online version of record will be different from this version once it has been copyedited and typeset.

PLEASE CITE THIS ARTICLE AS DOI: 10.1063/1.5133023

$$\begin{aligned}
 I_{D,OC} &= \int_s \frac{\partial \mathbf{D}}{\partial t} \cdot \mathbf{n} dS = \int_s \frac{\partial D_z}{\partial t} dS \\
 &= + \frac{\sigma_T}{4\pi} (z + z_{0^-}) \frac{\partial}{\partial t} \left[\int_{-\infty}^{\infty} dx \int_{-\infty}^{\infty} dy \int_0^{a(t)} dx' \int_{-b/2}^{b/2} \frac{dy'}{((x-x')^2 + (y-y')^2 + (z-z_{0^-})^2)^{3/2}} \right] \\
 &\quad - \frac{\sigma_T}{4\pi} (z - z_{0^-}) \frac{\partial}{\partial t} \left[\int_{-\infty}^{\infty} dx \int_{-\infty}^{\infty} dy \int_L^{L+a(t)} dx' \int_{-b/2}^{b/2} \frac{dy'}{((x-x')^2 + (y-y')^2 + (z-z_{0^-})^2)^{3/2}} \right] \\
 &\quad - \frac{\sigma_T}{4\pi} (z - z_1) \frac{\partial}{\partial t} \left[\int_{-\infty}^{\infty} dx \int_{-\infty}^{\infty} dy \int_0^{a(t)} dx' \int_{-b/2}^{b/2} \frac{dy'}{((x-x')^2 + (y-y')^2 + (z-z_1)^2)^{3/2}} \right] \\
 &\quad + \frac{\sigma_T}{4\pi} (z + z_2) \frac{\partial}{\partial t} \left[\int_{-\infty}^{\infty} dx \int_{-\infty}^{\infty} dy \int_L^{L+a(t)} dx' \int_{-b/2}^{b/2} \frac{dy'}{((x-x')^2 + (y-y')^2 + (z-z_2)^2)^{3/2}} \right] \\
 &\quad - \frac{1}{4\pi} (z - z_1) \frac{\partial}{\partial t} \left[\sigma_E(t) \int_{-\infty}^{\infty} dx \int_{-\infty}^{\infty} dy \int_{a(t)}^L dx' \int_{-b/2}^{b/2} \frac{dy'}{((x-x')^2 + (y-y')^2 + (z-z_1)^2)^{3/2}} \right] \\
 &\quad + \frac{1}{4\pi} (z + z_2) \frac{\partial}{\partial t} \left[\sigma_E(t) \int_{-\infty}^{\infty} dx \int_{-\infty}^{\infty} dy \int_{a(t)}^L dx' \int_{-b/2}^{b/2} \frac{dy'}{((x-x')^2 + (y-y')^2 + (z-z_2)^2)^{3/2}} \right] \quad (2)
 \end{aligned}$$

When $z = 0$, $I_{D,OC}$ through the triboelectric charge surface is given by (Supplementary Note 2):

$$I_{D,OC} = b \frac{d((L-a(t))\sigma_E(t))}{dt} = b(L-a(t)) \frac{d\sigma_E(t)}{dt} - b\sigma_E(t) \frac{da(t)}{dt} \quad (3)$$

2.2 Output performance at short-circuit condition

For SC conditions, charges will be transferred from one electrode to another to maintain electrostatic equilibrium; we assume that the transferred charge density between the two electrodes is $\pm \sigma_U(t)$. As a result, the charge density on the overlapping area is $\sigma_E(t) + \sigma_U(t)$ (z_0^- position), $-\sigma_E(t) - \sigma_U(t)$ (z_0^+ position), respectively. The electric field Eq. (1) can be rewritten as:

$$\begin{aligned}
 \mathbf{E}(x, y, z, t) = & -\frac{\sigma_T}{4\pi\epsilon(\mathbf{r})} \int_0^{a(t)} dx' \int_{-b/2}^{b/2} dy' \frac{(x-x', y-y', z-z_0)}{((x-x')^2 + (y-y')^2 + (z-z_0)^2)^{3/2}} \\
 & + \frac{\sigma_T}{4\pi\epsilon(\mathbf{r})} \int_L^{L+a(t)} dx' \int_{-b/2}^{b/2} dy' \frac{(x-x', y-y', z-z_0)}{((x-x')^2 + (y-y')^2 + (z-z_0)^2)^{3/2}} \\
 & + \frac{\sigma_T}{4\pi\epsilon(\mathbf{r})} \int_0^{a(t)} dx' \int_{-b/2}^{b/2} dy' \frac{(x-x', y-y', z-z_1)}{((x-x')^2 + (y-y')^2 + (z-z_1)^2)^{3/2}} \\
 & - \frac{\sigma_T}{4\pi\epsilon(\mathbf{r})} \int_L^{L+a(t)} dx' \int_{-b/2}^{b/2} dy' \frac{(x-x', y-y', z-z_2)}{((x-x')^2 + (y-y')^2 + (z-z_2)^2)^{3/2}} \\
 & + \frac{\sigma_E}{4\pi\epsilon(\mathbf{r})} \int_{a(t)}^L dx' \int_{-b/2}^{b/2} dy' \frac{(x-x', y-y', z-z_1)}{((x-x')^2 + (y-y')^2 + (z-z_1)^2)^{3/2}} \\
 & - \frac{\sigma_E}{4\pi\epsilon(\mathbf{r})} \int_{a(t)}^L dx' \int_{-b/2}^{b/2} dy' \frac{(x-x', y-y', z-z_2)}{((x-x')^2 + (y-y')^2 + (z-z_2)^2)^{3/2}} \\
 & + \frac{\sigma_U}{4\pi\epsilon(\mathbf{r})} \int_{a(t)}^L dx' \int_{-b/2}^{b/2} dy' \frac{(x-x', y-y', z-z_1)}{((x-x')^2 + (y-y')^2 + (z-z_1)^2)^{3/2}} \\
 & - \frac{\sigma_U}{4\pi\epsilon(\mathbf{r})} \int_{a(t)}^L dx' \int_{-b/2}^{b/2} dy' \frac{(x-x', y-y', z-z_2)}{((x-x')^2 + (y-y')^2 + (z-z_2)^2)^{3/2}} \quad (4)
 \end{aligned}$$

The displacement current through the entire surface z at SC conditions ($I_{D,SC}$) is determined by

$$\begin{aligned}
 I_{D,SC} = & \int_s \frac{\partial \mathbf{D}}{\partial t} \cdot \mathbf{ndS} = \int_s \frac{\partial D_z}{\partial t} dS \\
 = & -\frac{\sigma_T}{4\pi} (z-z_0) \frac{\partial}{\partial t} \left[\int_{-\infty}^{\infty} dx \int_{-\infty}^{\infty} dy \int_0^{a(t)} dx' \int_{-b/2}^{b/2} \frac{dy'}{((x-x')^2 + (y-y')^2 + (z-z_0)^2)^{3/2}} \right] \\
 & + \frac{\sigma_T}{4\pi} (z-z_0) \frac{\partial}{\partial t} \left[\int_{-\infty}^{\infty} dx \int_{-\infty}^{\infty} dy \int_L^{L+a(t)} dx' \int_{-b/2}^{b/2} \frac{dy'}{((x-x')^2 + (y-y')^2 + (z-z_0)^2)^{3/2}} \right] \\
 & + \frac{\sigma_T}{4\pi} (z-z_1) \frac{\partial}{\partial t} \left[\int_{-\infty}^{\infty} dx \int_{-\infty}^{\infty} dy \int_0^{a(t)} dx' \int_{-b/2}^{b/2} \frac{dy'}{((x-x')^2 + (y-y')^2 + (z-z_1)^2)^{3/2}} \right] \\
 & - \frac{\sigma_T}{4\pi} (z-z_2) \frac{\partial}{\partial t} \left[\int_{-\infty}^{\infty} dx \int_{-\infty}^{\infty} dy \int_L^{L+a(t)} dx' \int_{-b/2}^{b/2} \frac{dy'}{((x-x')^2 + (y-y')^2 + (z-z_2)^2)^{3/2}} \right] \\
 & - \frac{\sigma_E}{4\pi} (z-z_1) \frac{\partial}{\partial t} \left[\int_{-\infty}^{\infty} dx \int_{-\infty}^{\infty} dy \int_{a(t)}^L dx' \int_{-b/2}^{b/2} \frac{dy'}{((x-x')^2 + (y-y')^2 + (z-z_1)^2)^{3/2}} \right] \\
 & + \frac{\sigma_E}{4\pi} (z-z_2) \frac{\partial}{\partial t} \left[\int_{-\infty}^{\infty} dx \int_{-\infty}^{\infty} dy \int_{a(t)}^L dx' \int_{-b/2}^{b/2} \frac{dy'}{((x-x')^2 + (y-y')^2 + (z-z_2)^2)^{3/2}} \right] \\
 & + \frac{\sigma_U}{4\pi} (z-z_1) \frac{\partial}{\partial t} \left[\int_{-\infty}^{\infty} dx \int_{-\infty}^{\infty} dy \int_{a(t)}^L dx' \int_{-b/2}^{b/2} \frac{dy'}{((x-x')^2 + (y-y')^2 + (z-z_1)^2)^{3/2}} \right] \\
 & - \frac{\sigma_U}{4\pi} (z-z_2) \frac{\partial}{\partial t} \left[\int_{-\infty}^{\infty} dx \int_{-\infty}^{\infty} dy \int_{a(t)}^L dx' \int_{-b/2}^{b/2} \frac{dy'}{((x-x')^2 + (y-y')^2 + (z-z_2)^2)^{3/2}} \right] \quad (5)
 \end{aligned}$$

If $z = 0$ is chosen to evaluate $I_{D,SC}$, Eq. (5) becomes (Supplementary Note 2):

$$I_{D,SC} = b(\sigma_E(t) - \sigma_U(t)) \frac{da(t)}{dt} + b(L - a(t)) \left(\frac{d\sigma_U(t)}{dt} - \frac{d\sigma_E(t)}{dt} \right) \quad (6)$$

Moreover, since the two electrode potentials are the same at SC conditions, we have $\phi_1(x, y, z_1, t) = \phi_2(x, y, z_2, t)$. So, the transferred charges $\sigma_U(t)$ can be obtained. The capacitance of the LS TENG can now be calculated in the standard way as the ratio between charge and voltage across the capacitor (Supplementary Note 1).

2.3 Alternating current output performance

2.3.1 The electric potential and Kirchhoff's law

In the general case where a resistor is connected to the electrodes, the electric potential at the positions z_1 $\phi_1(x, y, z_1, t)$ and z_2 $\phi_2(x, y, z_2, t)$, respectively, are different. According to Kirchhoffs' law, the governing equation

$$-ZA \frac{d\sigma_U}{dt} = \phi_1(x, y, z_1) - \phi_2(x, y, z_2) \quad (7)$$

where Z is the external electrical impedance, A is the contacting surface, $\sigma_U(t)$ is the free charge density, $Q_u = A\sigma_U(t)$ is the transferred charge between the two electrodes, and the potential over Z is ZdQ_u/dt . Note that Eq. (7) is a time-dependent differential equation, from which $\sigma_U(t)$ can be evaluated. Then, the conduction current ($I(t)$), instantaneous power ($P(t)$), output energy ($E(t)$), and average power output (P_{av}) can be obtained (Supplementary Note 3).

2.3.2 Relaxation time and the final cycle k

Similar to the typical ZC series circuit, the transient period between two steady states depends on the time constant $\tau = ZC$. For TENGs, due to movements of charges, the total capacitance changes in time. However, as we have proved before,¹² there are two characteristic time constants: τ_0 and $\tau_{x_{max}}$, where $\tau_0 = ZC_0$, and $\tau_{x_{max}} = ZC_{x_{max}}$; C_0 and $C_{x_{max}}$ stand for the total capacitance of TENGs at $x = 0$ and $x = x_{max}$, respectively. This means the time constant τ of TENGs changes between τ_0 and $\tau_{x_{max}}$. Here, the relaxation time (τ_{relax}) is closely related to the variation of total capacitance of TENGs, or more accurately, directly related to the effective capacitance (root-mean-square (*rms*)) value of TENGs (C_{rms}), refer to the text below (taking the LS mode TENG as an example).

The effective capacitance of C_{ac} ($C_{ac,rms}$) is derived from:

$$C_{ac(rms)} = \sqrt{\frac{1}{T} \int_0^T (C_{ac}(t))^2 dt} \quad (8)$$

where C_{ac} is $\frac{\epsilon_0 b a_{max}}{2d_0} \cos(\omega t)$, which is a function of time, and T is the period of C_{ac} (Supplementary Note 4). In fact, the effective value of any quantity plotted as a function of time can be found by using the above equation.^{30,31} Then, the effective value of $C(t)$ is obtained through Eq. (8), we have

$$C_{rms} = \sqrt{C_{in}^2 + (C_{ac(rms)})^2} \quad (9)$$

where C_{in} is $\frac{\epsilon_0 b}{d_0} (l - \frac{a_{max}}{2})$; this is a fixed value, representing the DC component or the average value of $C(t)$ (Supplementary Note 4). In other words, the total capacitance of the LS mode TENG has both the DC component and AC component determined by the structure of the TENG. This special characteristic leads to a profound difference between the AC output of TENG and a traditional sinusoidal AC power generator, the details of which will be discussed below.

More importantly, in a DC network, it is a fact that the current/voltage of a capacitive approaches zero after about five time constants (ZC). This conclusion is also applicable for a TENG circuit. Therefore, we can easily obtain the τ_{relax} of a TENG, which is $\tau_{relax} = 5ZC_{rms}$ (Eq. (S30c)); and then the corresponding needed minimum number of cycles k_{relax} is:

$$k_{relax} = \frac{\tau_{relax}}{T} \quad (10)$$

indicating that after k_{relax} cycles the TENG is effectively in a steady state situation. Here, the relevant minimum integer N that the TENG needs to reach steady state is defined by $N = \text{Int}(k_{relax})$. *Int* implies rounding up the argument to the nearest integer. While simple, this result is important and applicable to all other types of TENGs despite their different configurations and triggering conditions.

2.3.3 Optimum resistance in steady state

From previous work, we know that the TENG is represented through a time-varying capacitor ($C(t)$) and an open-circuit voltage source (V_{oc}).³² In general, the opposition of a capacitor to the flow of charge is called the reactance which results in the continual interchange of energy between the source and the electric field of the capacitor. For the TENG, $C(t)$ also

offers resistance to the flow of electric charges, i.e., converting mechanical energy into electrical energy stored in $C(t)$. As for the ideal conductor the time-varying capacitor does not dissipate energy. Here, the capacitive reactance or the internal resistance of the TENG ($Z_T(t)$) is defined by:

$$Z_T(t) \equiv \frac{1}{\omega C(t)} = \frac{1}{2\pi f C(t)} \quad (11)$$

where ω is the angular velocity, and f is the frequency of the $C(t)$. Usually, the change of $C(t)$ will result in a change of $Z_T(t)$ during the energy conversion process. While the magnitude of the mechanical source varies in different ways, $Z_T(t)$ of TENGs can be calculated by Eq. (11). We can easily prove that for the TENG, $Z_T(t+T) = Z_T(t)$ and $Z_T(t) = Z_T(-t)$, revealing that this function is a periodic and even function (Supplementary Note 4). Besides, according to the Fourier theorem, a periodic function of frequency ω can be expressed as an infinite sum of sine and cosine functions that are integral multiples of ω . Evidently, an even function contains no sine terms thus $Z_T(t)$ can be expressed as a Fourier cosine series,

$$Z_T(t) = a_0 + \sum_{n=1}^{\infty} a_n \cos(n\omega t) \quad (12)$$

where $a_0 = \frac{2}{T} \int_0^{T/2} Z_T(t) dt$ and $a_n = \frac{4}{T} \int_0^{T/2} Z_T(t) \cos(n\omega t) dt$. The coefficient a_0 is the DC component of $Z_T(t)$, the coefficients a_n is the Fourier coefficients representing the amplitude of the various AC components with frequency $n\omega$. Eq. (12) reveals the difference between $Z_T(t)$ and the reactance of a traditional capacitor (X_C). Evidently, the Fourier series of a periodic function $Z_T(t)$ resolves $Z_T(t)$ into a DC component and AC component, where the latter is composed of an infinite series of harmonics.

As in the case for the effective capacitance, the *rms* value/effective value of $Z_T(t)$ is

$$Z_{opt} = Z_{rms} = \sqrt{\frac{1}{T} \int_0^T (Z_T(t))^2 dt} \quad (13)$$

where T represents the period of $Z_T(t)$. This concept of optimizing Z is in contrast to the typical case in the literature where the load resistance is optimized from a relaxation state (or from the first half cycle).^{11,13,18-19} In general, if the *rms* of an AC signal has the same value as a DC signal then the two signals dissipate the same amount of power in a circuit. Therefore, Z_{rms} can be

regarded as the optimum resistance of a TENG. Indeed, when a loading resistor equal to Z_{rms} is coupled to the TENG, the maximum output power is obtained. Therefore, Z_{rms} is called the optimum resistance of TENGs. Moreover, from Eqs. (S31) and (13), we find that Z_{opt} is a function of geometry and motion parameters such as the motion frequency and maximum separation distance.

2.3.4 Effective output and the average power

Subject to periodic mechanical motion, the TENG eventually reaches the steady state resulting in steady power output. Similar to the basic analysis of the C_{rms} and Z_{rms} , the effective output of TENGs (equivalent to the DC value) can be defined (Supplementary Note 5). More importantly, we have proved that the relationship between the average power (P_{av}) and the product of V_{rms} and I_{rms} is:

$$P_{av} = V_{rms} I_{rms} \quad (14)$$

where V_{rms} , I_{rms} represent the *rms*/effective voltage, and current of TENGs, respectively. The detailed proofs are provided in part 3.3. Eqs. (14) and (S32a)-(S32d) are regarded as the basic effective output of TENGs. At any time during the positive and negative half periods of the AC current, power is being delivered to the resistor. These equations establish a particular level of power transfer for the full cycle, so that we do not have to determine the level of power to apply to a quantity that varies in time.

2.3.5 Figure-of-merits in steady state (FOM_T)

As mentioned above, effective values are utilized to describe the basic effective output performances of TENGs. To compare and evaluate each TENGs' unique output characteristic, the figure-of-merit of TENGs in steady state (FOM_T) is proposed, which is defined as (Supplementary Note 6):

$$FOM_T = \frac{2\varepsilon_0 E_{ac,opt}}{\sigma^2 A x_{max}} = \frac{2\varepsilon_0 (V_{rms} I_{rms})_{Z=Z_{opt}}}{\sigma^2 A x_{max} f} \quad (15)$$

where $E_{ac,opt}$ is the largest output energy in the steady state, V_{rms} and I_{rms} are the effective voltage and current for a load of Z_{opt} , respectively; A is the contacting surface area, and f stands for the frequency of TENGs in steady state.

Note that the FOM_T is very different from the $FOMs$ presented in literature Ref.15, and

also different compared to the FOM_{RS} proposed before.¹⁰ Firstly, the $FOMs$ is defined by Zi et al, considering the values of V_{oc} and transferred charges at SC conditions, is much bigger than the output of TENGs, when a resistor is connected. We present a discussion of FOM_{RS} and show that the latter primarily depends on the optimum resistor. Moreover, the FOM_T is defined for steady state operation and the governing parameters, obtained from the experiments, indicate a simple practical way to optimize the power output. From Eqs. (9), (11) and (13), it follows that once a TENG is designed, only one relevant motion condition (for example the frequency) is needed to obtain the largest output performance.

2.4 Dimensionless analysis and the Governing Equation

In general, dimensional analysis will often give good insight into the physics we analyze. The motivation behind dimensional analysis is that any dimensionally equation can be written in an entirely equivalent non-dimensional form. Here we use this method to study more generally our 3D mathematical model and the AC output of TENGs (Supplementary Note 7). Moreover, a change in any parameter of a TENG gives rise to new specific conditions for the optimal output performance. Here, a multi-parameter case is conveniently investigated using dimensional analysis. This method is effectively used to find the optimum conditions in for maximizing output. We shall use it to derive the non-dimensional form of the governing equation of TENGs and conditions. By different scaling parameters, we define a series of dimensionless parameters: transferred charge (Q_u^*), resistance (Z^*) time/phase angle (t^* or φ), and electric potential (ϕ^*). Then the governing equation of Eq. (7) becomes:

$$-Z^* \frac{dQ_u^*}{dt^*} = \phi_1^* - \phi_2^* \quad (16)$$

Eq. (16) is the dimensionless form of the governing equation of TENGs. With the initial condition $Q_u^*(0) = 0$, the analytical solution of Q_u^* can be obtained (Supplementary Note 7).

Moreover, we can also derive the dimensionless capacitance (C^*), current (I^*), power (P^*), average power (P_{ave}^*) and electric energy (E^*) delivered to the external resistor Z^* (Supplementary Note 7). Note that normalizing the equations and conditions in part 2.4 allows us to get a reduction in the number of parameters. Based on the above analysis, we obtain dimensionless parameters such as the effective dimensionless transferred charge ($Q_{u,ms}^*$), current (I_{ms}^*), voltage (V_{ms}^*), power (P_{ms}^*), electric energy (E_{ms}^*), electric displacement current (D^*),

displacement current (I_D^*), displacement current density (J_D^*) and so on (Supplementary Note 8).

3. RESULTS AND DISCUSSION

3.1 FEM simulation and basic output at OC and SC conditions

The displacement current is the fundamental concept in the theory of TENGs.^{7,11} Therefore, we put our focus on the variation of the electric field E and electric displacement D as well as polarization P (where $P = (\epsilon - \epsilon_0)*E$) in TENGs. Using the finite element method (FEM), a series of results is obtained at OC conditions as demonstrated in Fig. 1. The specified parameters are listed in Table S1, which is the same value as we used in the MATLAB numerical calculations. Fig. 1(a) is a sketch of a typical dielectric-to-dielectric LS mode TENG we analyzed using FEM mode. The charge density on the contacting surfaces is zero because the distance between the generated tribocharges with opposite signs is very small.¹⁹ The charge densities at z_1 and z_2 position of the overlapping area are $+\sigma_{E_1}$ and $-\sigma_{E_2}$, respectively, which are found from Eq. (S12). The distributions of the electric field and electric displacement components (E_z and D_z) along the z -direction for different x_{\max} are illustrated in Fig. 1(b) and 1(c), respectively. When $a(t)$ increases from 0 to x_{\max} , the E_z at position z_1 (non-overlapping area) decreases and then abruptly increases until it approaches a plateau. The decrease trend is mainly due to a number of negative charges accumulating at the overlapping areas at the z_1 and z_2 positions so as to ensure the condition of electrostatic equilibrium. But the total charges on the metal electrodes must be zero as pointed out earlier. E_z at the z_2 position behaves in a similar way to E_z at the z_1 position but the former is characterized by a lower maximum value. This is because the relative permittivity of the bottom dielectric material (ϵ_1) is only half of the top dielectric material (ϵ_2), and the relative displacement occurs between the two sliding bars. As demonstrated in Fig. S1(c), some representative points have been detected. For instance, the same trend can be observed at the 0.05 X/L point (z_1 position) and 0.95 X/L point (z_2 position). A similar tendency is found for the electric displacement as shown in Fig. 1(b).

At the maximum $x_{\max} = 0.8 X/L$, the distributions of D_z , E_z and P_z are shown in Fig. d1, d2 and d3, respectively. It is seen that D_z , E_z and P_z inside the dielectric exhibit the same direction at the overlapping area. The relationship among them is demonstrated in Fig. S1(a), i.e., $D_z =$

This is the author's peer reviewed, accepted manuscript. However, the online version of record will be different from this version once it has been copyedited and typeset.

PLEASE CITE THIS ARTICLE AS DOI: 10.1063/1.5133023

$\epsilon_0 E_z + P_z$. When the top sliding bar moves, a large number of charges have to accumulate at the overlapping area according to Eq. (S12). This means that a dramatic change of the electric field occurs at the dielectric-electrode interface at z_1 and z_2 position. The variations of E_z (e), P_z (f), and D_z (g) inside the dielectric material are also simulated and illustrated in Fig. 1(e), 1(f), 1(g), corresponding to the position of red line in Fig. S1(b). It is seen that the E_z field components in dielectric 1 and dielectric 2 are different, and a sudden increase across the interface is observed. A similar trend with an abrupt increase happens for P_z , but P_z in the bottom dielectric is bigger than that at the top dielectric. In contrast, the magnitude of D_z in dielectric 1 is equal to the magnitude of D_z in dielectric 2, i.e., continuity of D_z is found at the interface in accordance with the boundary conditions for the normal electric displacement component. In addition, according to the Eq. (S12), free charges will accumulate at the overlapping area especially for a large x_{\max} , which results in a stronger polarization of the dielectric, a larger electric field and electric displacement, as demonstrated in Fig. 1(g). D_z and P_z at position z_1 and P_z at position z_2 are shown in Fig. S1. It should be noticed that the electric displacement must vanish on the dielectric-electrode interface due to the distribution of free charges.

At SC conditions, the variations of E_z (Fig. 2(a)), D_z (Fig. 2(b)), and P_z (Fig. 2(c)) are clearly different compared to those at OC conditions. E_z at the z_1 and z_2 positions exhibit an abrupt increase and then saturates at its maximum value. However, the saturated value of E_z at the z_1 position is twice as large as that at the z_2 position since ϵ_1 is only a half the value of ϵ_2 . The total electric displacement is discontinuous at the interface due to the presence of free charges. Fig. S1(f) reveals that $D_z = \epsilon_0 E_z + P_z$. This result applies to both OC and SC conditions (Fig. S1(a), and Fig. S3(a)). Furthermore, taking the D_z field at the z_1 position as an example, we find a negative D_z that increases in magnitude, and then exhibits a sudden increase (in magnitude) for OC conditions (Fig. 1(c)). For SC conditions, a different behavior is observed: D_z is positive and shows an abrupt increase (Fig. 2(b)). Under SC conditions, electrons flow between the two electrodes reduces the potential difference and ensures the electrostatic equilibrium. At OC conditions, there is no charges transferred between the two electrodes. To maintain a zero total charge at each electrode, a large number of electrons accumulate at the overlapping area of the dielectric-electrode interfaces, resulting in a stronger overall electric field and a larger polarization magnitude.

The numerical calculations of E_z at the z_1 and the z_2 positions using our quasi-analytical 3D model are similar to the FEM simulations as depicted in Fig. 2e and Fig. S4. Further, a comparison was carried out between the present 3D model and the previously published capacitance model (CA model).¹⁷ From the transferred charges and current at the SC condition plots (Fig. 2(f) and 2(g)), it is apparent that the two methods agree thereby demonstrating the correctness and validity of the 3D model. In particular, this model has shown its advantage in terms of offering a more clear physical picture of TENG operation from the viewpoint of classical electrodynamics. The displacement current I_D was also simulated subject to SC and OC conditions as illustrated in Fig. 2(h) and 2(i). The variation of I_D ($I_{D,sc}$) is identical to that of the current (I_{sc}) at SC conditions. Interestingly, the magnitude of I_D at OC conditions ($I_{D,oc}$) is equal to $I_{D,sc}$ yet it displays a phase change. This is can be explained by the following two reasons.

Firstly, it is well known that I_D is defined as the rate of change of the electric displacement (D), while D is associated with electric field E as $D = \epsilon E$. For the LS mode TENG at SC conditions, when the upper bar starts to move, charges will flow from the bottom electrode to the top electrode leading to a reduced potential difference. Secondly, subject to OC conditions, no charges can transfer from the external circuit of TENGs. As the upper bar moves, the electric field generated by the triboelectric charges yields a polarized dielectric. To ensure electrostatic equilibrium, the electric field is shielded by the free/image charges on each electrode. In particular, when the separation distance increases, charges accumulate on the overlapping area so as to keep the total numbers of positive and negative charges on the electrode equal to each other. Thus, more charges are accumulated at the overlapping area leading to an increase in the electric field in the plane of contacting surface, but along the opposite direction (Fig. 1(b) and 1(c)). The end result is an $I_{D,oc}$ in opposite phase compared with the $I_{D,sc}$ subject to SC conditions. Furthermore, a comparison of electric potential and potential differences between the 3D model and FEM simulations are demonstrated in Fig. S3(b) and S3(d), respectively. We notice that perfect agreement is found. More importantly, it is clear that there exists a big offset from zero of the potential differences (V_{oc}) in Fig. S3(b). However, for a traditional sinusoidal current, it always reverses at regular time intervals and has alternately positive and negative values, and its average value is zero. So there is a big difference between the basic output of

the LS mode TENG and a traditional sinusoidal AC power generator. This phenomenon can also be found in the contact-separation and single-electrode mode TENG, which is mainly due to the DC component in $C(t)$, as mentioned in part 2.3.2.^{9,14,18} Besides, the potential peak at different x_{\max} is also calculated as shown in Fig. S3(c). It is apparent that the potential peak increases as the maximum x_{\max} increases. This trend was also found in the previous published model.¹⁹

3.2 AC output at different loading conditions

We have systematically simulated the AC output of the LS mode TENG according to the developed quasi-analytical 3D model. By use of Eq. (7), the charge transfer process at different loading conditions (from $Z = 5 \times 10^7 \Omega$ to $Z = 1 \times 10^9 \Omega$) has been calculated as indicated in Fig. 3(a)-3(e). It is clear that the output performance is between the results associated with OC and SC conditions, as one would expect. In Fig. 3(a)-3(e), the relaxation state and steady state are remarkable different. The response approaching steady state changes with different load resistors. For instance, when Z is $5 \times 10^7 \Omega$, the relaxation time τ is 0.091s and the minimum needed cycle is 1, which means that after 0.091s or at least 1 cycle the TENG reaches steady state. However, when Z increases to $1 \times 10^9 \Omega$, the minimum needed cycle is 12 cycles, and the relaxation time increases to 1.838s, being much longer than that of a small resistor.

This is due to the following reasons. Firstly, the loaded resistor offers resistance to the flow of charges between the two electrodes leading to a slower charge transfer rate than that at SC conditions (Fig. 2(f)). Taking the $Z = Z_{\text{opt}}$ ($Z_{\text{opt}} = 1.19 \times 10^8 \Omega$) as an example (Fig. 3(b), Fig. 4(a) and 4(b)), when the upper sliding bar starts to move from the left to right, the electric field generated by the tribocharges move in the dielectric, inducing electrons at the dielectric-electrode interface, leading to a potential difference between the two electrodes. To decrease this potential difference, electrons transfer rapidly from the bottom electrode to the top one. However, due to the resistance caused by the load resistor, the electron transfer rate is lower than that at SC conditions. As the total transfer of electrons increase, the relevant total electric field and potential difference decrease (Fig. 4(b)), leading to a gradual decrease of the charge transfer rate (Fig. 3(b) and Fig. 4(a)), then generating a peak voltage and current (Fig. 4(a) and 4(b)). After the upper sliding bar reaches x_{\max} , charge transfer still occurs but at a slower rate. When the upper bar starts to reverse, the total electric field and potential difference decrease to

0 and then increase in the reverse direction. As a result, charges transfer from the top electrode to the bottom one leading to a peak charge during the transfer process. Similarly, the loaded resistor will reduce the charge transfer rate again. After many cycles, the frequency of charge transfer is equivalent to the characteristic frequency of the mechanical motion, i.e., the TENG system reaches steady state. For the relaxation state, the situation is markedly different as mentioned above.

On the other hand, as discussed in part 2.3.2, the charge transfer process between the two electrodes is analogous to the charging/discharging process of a traditional ZC series circuit. From Eq. (9), we obtain $C(t)$ and its *rms* value as shown in Fig. 3(f). Initially, there is a larger C_0 at $x = 0$; when $x(t)$ increases, the corresponding $C(t)$ decreases until it reaches its minimum value $C_{x_{\max}}$, the process of which is equivalent to a charging/discharging process in the ZC circuit. On the contrary, the process can be regarded as a discharging/charging process. From Eq. (S30c), we can calculate an approximate time constant/relaxation time during the AC output process. The relaxation time depends on both of the loaded resistor and effective value of $C(t)$. Eqs. (9) and (S30c) describe well the relaxation state of TENGs. For instance, as shown in Fig. 3(e), a clear difference in the transferred charge from the relaxation state to steady state is found. In fact, even in steady state, the plot of the charge transfer is not a pure sinusoidal curve.

The internal resistance and optimum resistance of the LS mode TENG are plotted in Fig. 3(g). We observe a DC component in the AC signals. Although the AC plot is not a pure cosine curve, it is periodic with the characteristic frequency of ω . As discussed in part 2.3.3, the effective value of $Z_T(t)$ is equal to Z_{opt} of the LS mode TENG. Fig. 3(b) depicts the transferred charge-time relationship for Z_{opt} , we will prove latter that the largest output occurs for Z_{opt} . The relaxation time and minimum needed cycles with different load resistors are shown in Fig. 3(h). Fig. 3(i) shows the influence of x_{\max} on the relaxation time and the ratio of $\tau_{\text{fixed}}/\tau_{\text{ac,rms}}$ for different Z_{opt} . The time τ increases with the increase of x_{\max} , which is attributed to the increase of C_{rms} , in agreement with Eq. (9). However, the ratio of $\tau_{\text{fixed}}/\tau_{\text{ac,rms}}$ decreases. Eqs. (8) and (S30a) reveal that τ_{fixed} decreases, but the $\tau_{\text{ac,rms}}$ decreases as x_{\max} increases, eventually reducing the ratio. In addition, the influence of x_{\max} on C_{fixed} and $C_{\text{ac,rms}}$ is shown in Fig. S5, from which we can clearly find that the C_{fixed} (or C_{in}) increases as x_{\max} increases. The relationship among Z_{opt} , frequency and x_{\max} are also discussed, as depicted in Fig. 3(j) and 3(k). Our results suggest that

Z_{opt} is directly proportional to the x_{max} (Fig. 3(k)) but inversely proportional to the frequency (Fig. 3(j)), and the frequency has a strong effect on Z_{opt} . For instance, when the frequency of TENGs increases to 1×10^8 Hz, the ideal Z_{opt} is approximately reduced to a small value 1Ω .

To investigate the relaxation state and steady state, the basic output performances, including the charge-time, current-time, voltage-time, power-time and energy-time relationships for $Z = Z_{\text{opt}}$ and $Z = 1 \times 10^9 \Omega$, are calculated using Eqs. (7), and (S24)-(S26). As shown in Fig. 4(a), the point *A* in the charge curve represents the relaxations time, which is 0.218 s. This means that after 0.218 s, the TENG system reaches steady state, the corresponding frequency is equal to the characteristic frequency of the mechanical motion. Point *C* and point *E* stand for the second and third cycles and both period are 0.16 s, equivalent to the mechanical period. We notice that the charge at point *A* (Q_A), point *C* (Q_C) and point *E* (Q_E) are 28.62 nC, 28.69 nC, and 28.7 nC, respectively. Clearly, Q_C is almost equal to Q_E , indicating that the TENG is in steady state. Besides, as depicted in Fig. 3(a), point *B* in the current curve represents the first period of the TENG system, while point *D* and *F* stand for the second and third cycles, respectively. It is seen that the time at point *B* is 0.18 s, which is smaller than the relaxation time of 0.218 s, indicating that the TENG has not reached steady state. The time at point *D* and point *F* are 0.35s and 0.51s, respectively, and the period of each cycle is 0.16 s, proving again that the TENG is in steady state.

Using the same approach, we have investigated the basic AC output performance at a larger resistance of $1 \times 10^9 \Omega$, as shown in Fig. S6(a) and S6(b). When the load resistor increases, the relaxation time and corresponding needed cycle all increase. In particular, a general analysis of the power and energy in steady state is demonstrated. As shown in Fig. 4(b), during the positive and negative half periods of the AC current, power is delivered to the resistor. And the period of the power output for a load resistor Z_{opt} is equal to the period of voltage. This implies there are two different peak powers in one cycle attributed to the difference of C_0 and $C_{x\text{max}}$ for TENGs, resulting in the asymmetry of voltage and current, finally generating the different peak power at steady state. Moreover, the energy from the first half cycle is different from that of the second one. As illustrated in Fig. 4(b), the $\Delta E1$ representing the harvested energy at the first half cycle is 2.73 μJ , which is different compared to that of the second half cycle of 1.50 μJ (stands by $\Delta E2$).

On the other hand, after the TENG system reaches steady state, a detailed understanding of the phase relationships for different loading conditions is very important. In steady state, all of the basic output signals such as the charge, current, voltage have the characteristic frequency of the mechanical motion. Their output peak signals do not show any significant change, i.e., the maximum/minimum peak charge (Q_{mp}/Q_{np}), the positive/negative peak current (I_{pp}/I_{np}), the positive/negative voltage peak (V_{pp}/V_{np}), and the maximum/minimum peak power (P_{mp}/P_{np}). Moreover, the voltage and current are in phase both for relaxation state and steady state, as shown in Fig. 4(b), 4(d), and Fig. S6(b). This means that voltage and current are in phase. Nevertheless, the phase angle of the voltage (charge, or the current) changes with the load resistor. As depicted in Fig. 4(a) and 4(b), we find that the phase angle between the charge curve and current plot of Z_{opt} is 0. When the load resistor is lower than Z_{opt} , smaller time is needed to reach the peak charge; instead, when a load resistor larger than Z_{opt} is used, a longer time is needed. So the charge curve of the smaller resistance is said to lead the charge curve of Z_{opt} ; on the contrary, it lags the charge plot above Z_{opt} by some angle even though waveforms display the same frequency. The phase angle difference mainly comes from the “initial phase” difference (left figures in Fig. 4(c)), which is caused by the different resistance from the load resistor. Variations of the phase for transferred charges and current from the first cycle to steady state cycle at different load resistances are shown in Fig. S7 and Fig. S8. The same phenomena can be observed in Fig. 4(d) and 4(e). Fig. S6(c) illustrates the harvested energy from the first cycle to the steady state cycle with different load resistances, from which it is seen that the maximum energy is obtained under the Z_{opt} . Furthermore, the period and corresponding frequency in each cycle at relaxation state are extracted and illustrated in Fig. 4(f). The period decreases gradually as the increase of the operation cycle; however, the corresponding frequency displays an increase gradient until it becomes the mechanical frequency, indicating that the TENG system has reached in steady state. Hence one can tell if the TENG system is in a state of relaxation or at steady state and even how many more cycles are needed to reach steady state by the frequency of each cycle.

3.3 Effective value and the maximum average power

In AC outputs, the magnitude of charge (Fig. 5(a), Fig. S9(b)), current (Fig. S9(a) and Fig. S9(d)), and voltage (Fig. 5(b) and Fig. S9(c)) all vary with time. In order to obtain the

appropriate measure of current and voltage that represents the real effect, effective values are commonly used terms when discussing periodic signals. In general, rms is the most common method utilized to find the effective values of voltage or current while dealing with AC circuit.³¹ Using this approach, the Q_{rms} and V_{rms} at Z_{opt} and $5 \times 10^8 \Omega$ are calculated and demonstrated in Fig. 5(a) and 5(b), respectively. It should be recognized that there exists an offset from zero in each signal, directly indicating that a bias voltage, equivalent to a DC voltage, appears in the output signal besides the AC voltage component. This phenomenon is different compared to the traditional sinusoidal alternating current since the latter is completely symmetric about the x axis and the average value is zero. Therefore, there is an important difference between the LS mode TENG and the tradition sinusoidal AC power generator. However, for a freestanding mode TENG, an exact symmetry in the voltage/current relationship is found mainly attributed to its constant capacitance, even though the x_{max} changes.^{10,14,18} In Fig. 5(a), Q_{rms} at $5 \times 10^8 \Omega$ is about 38.33 nC, close to that of the Q_{rms} at Z_{opt} (35.83 nC. The relationship among Q_{rms} values at different load resistors in steady state shown in Fig. S10); but the Q_{steady} of the former shows a small variation range ($|Q_{\text{mp}}| - |Q_{\text{np}}|$). On the contrary, the V_{steady} of $5 \times 10^8 \Omega$ (Fig. 5(b)) demonstrates a larger variation range ($|V_{\text{pp}}| - |V_{\text{np}}|$) and a higher V_{rms} when compared to those at Z_{opt} . The same phenomenon is also observed from I_{rms} , as shown in Fig. S9(a). Notice that the reason of the small variation range of Q or large variation range of V with high resistance will be discussed latter.

The peaks of V_{rms} , I_{rms} and P_{av} in steady state under different load resistors are extracted and plotted in Fig. 5(c). With a relatively low resistance, the corresponding V_{rms} is lower, leading to a lower P_{av} . On the contrary, the I_{rms} decreases significantly at larger resistances, while the voltage increases, resulting in a small P_{av} again. However, for a load around $1 \times 10^8 \Omega$, both the V_{rms} and I_{rms} are in the transitional stage, and the maximum P_{av} is obtained in this region. So, three different working regions are predicted from these profiles, which is in good accordance with previous researches.^{13,17} More importantly, we can find that the P_{av} is equal to the product of V_{rms} and I_{rms} , which is $P_{\text{av}} = V_{\text{rms}} \times I_{\text{rms}}$. Then we can obtain the Eq. (14) in part 2.3.4. In particular, we also get the conclusions: $I_{\text{rms}} = V_{\text{rms}}/Z$, and $P_{\text{av}} = V_{\text{rms}}^2 \times Z$. The maximum P_{av} is obtained at the $1.19 \times 10^8 \Omega$, the resistance of which equals the result calculated by Eq. (13),

offering a direct evidence for the prediction that the *rms* value of $Z_T(t)$ can be regarded as the optimum resistance of TENGs. The P_{av} for the optimum resistance in steady state ($Z_{opt,steady}$) is about $26.65 \mu\text{W}$, which is improved by a factor of 77.5 % when compared to that at the optimum resistance calculated for the first half cycle ($Z_{opt,1half}$) (Fig. 5(d)). The bigger difference between the two P_{av} is due to the difference of the loaded optimum resistance. As depicted in Fig. 5(d), the Z_{opt} in the first cycle is $3.14 \times 10^8 \Omega$, while that at steady state is $1.19 \times 10^8 \Omega$, so clearly the two are significantly different. Obviously, we arrive at the conclusion that the optimum resistance of a TENG system is more appropriately calculated using the effective value of $Z_T(t)$ rather than from the first half cycle or in the relaxation state.

3.4 Relationship between the electric field and displacement current

We know that the generation of displacement current is due to the rate of change of the electric field, and the displacement current is the fundamental quantity of TENGs. Fig. 6(a) and 6(b) illustrate the electric field at z_1 position vs. time and relevant displacement current vs. time for a load Z_{opt} . Firstly, we find that both signals are always parallel and have the same frequency. When the electric field varies from the relaxation state to steady state, the relevant I_D changes simultaneously. But the two signals change with opposite phase as shown in Fig. 6(a) and 6(b). When comparing with the electric field for a resistance of $1 \times 10^9 \Omega$ (Fig. 6(c)), a small steady variation range of electric field and I_D are found. Increasing the load resistances results in an increase of the steady component of the charge, current, voltage and electric field, and the offset value from zero of each signal (similar to a DC component) is also improved, refer to Fig. 6(a), 6(b), and Fig. S11. As discussed before, a larger resistance leads to an increase of the relaxation time; however, within a limited time, only part of the free charges can flow between the electrodes, resulting in a small steady variation range of the transferred charges. More importantly, to ensure electrostatic equilibrium, more charges must accumulate at the overlapping area of the two sliding bars, making the potential difference between the two electrodes higher, again leading to a larger offset value from the 0. It is expected that a small variation of the transferred charge and the effective voltage is obtained for a high resistor value, i.e., close to OC conditions.

The temporal behavior of the displacement current I_D from the first cycle to the steady state cycle shown in Fig. 6(e) is identical to the change of the conduction current, refer to Fig.

4(d). Fig. 6(f) shows the change of electric field at z_1 position. It is found that the electric fields under various load resistors are different to each other even in the same cycle, and their trends in changes show good resemblance with those of I_D . A comparison was carried out between the electric field at z_1 and z_2 positions for the load resistance Z_{opt} , as illustrated in Fig. 6(g). We notice that the variation of electric fields display the same phase both for the first cycle and at steady state, but clearly with different magnitudes. In fact, the electric field contribution from charges at the z_2 position/top electrode is shielded due to distributed free charges at the bottom dielectric-electrode interface. Hence, a different magnitude of electric field occurs. Another reason is the different permittivity of the two dielectrics as mentioned before.

3.5 Dimensional analysis

A dimensional analysis often enables one to predict the behavior of large systems from a study of small-scale models. It can also provide a useful cataloging system of physical quantities. Fig. S12(a) and S12(b) demonstrate the dimensionless charge Q^* vs. phase angle φ and the dimensionless voltage V^* vs. φ from the first cycle to a steady state cycle subject to different dimensionless load resistors Z^* , respectively. Evidently, these results show similar profiles to the real charge/voltage tendency demonstrated in Fig. 4(c) and S7. Besides, the Q^*V^* plots from the first cycle and steady state cycle are illustrated in Fig. 7(a) and 7(b), respectively. From Fig. 7(a) we cannot get the closed Q^*V^* plot, in particular with a larger Z^* . However, these Q^*V^* plots in steady state are always closed both for a lower Z^* ($Z_1^* = 0.044$) and a higher Z^* ($Z_2^* = 4.353$). The largest Q^*V^* plot is obtained when Z_{opt}^* is 0.518, i.e., we can predict the largest dimensionless P_{av}^* and the largest E^* . Furthermore, the basic dimensionless parameters such as Q^* , I^* , V^* , P_{av}^* , E^* at different dimensionless distance of x_{max}^* are depicted in Fig. S12-S13 and Fig. 7(c). It is seen that these parameter outputs increase with the increase of the x_{max}^* . This is easy to understand since more charges can flow between the electrodes at a larger x_{max}^* . Moreover, the effective dimensionless parameters also increase with the increase of x_{max}^* (Fig. S12(c)-S12(e), and Fig. S13(c)).

As discussed above, we have derived the structural figure-of-merit of TENGs at steady state (FOM_T). Before that, the maximum dimensionless average power ($P_{av,max}^*$) at various x_{max} must be calculated as shown in Fig. S14, and the corresponding average power is depicted in Fig. S13(d). Fig. 7(d) depicts the structure figure-of-merits of the LS mode TENG at different

x_{\max} . When x_{\max} increases, $P_{\text{av,max}}^*$ increases simultaneously, resulting in an increase of FOM_T and consistent with the structural figure-of-merit of TENGs for an infinite resistance or/and subject to the optimum resistance calculated from the first half cycle (FOM_S and FOM_{RS}).^{10,15} Note that the plot of FOM_T is smaller than that of the FOM_S and FOM_{RS} , since the relevant harvested energy is lower at steady state, all free charges are not transferred in one cycle. However, for the FOM_S and FOM_{RS} , where all free charges are transferred in a cycle, leading to a larger magnitude of energy output results during one operation cycle. We believe that the strategy for deriving FOM_T at steady state of the LS mode TENG is applicable to other types of triboelectric nanogenerators with a time-varying capacitance.

Although this 3D model can describe the planar geometry of TENGs directly, for a non-planar geometry such as a convex-concave surface, it can be convenient to recast the problem using eg. cylindrical or spherical coordinates or other coordinate systems. On the other hand, the important feature of the TENG is that the electric field is a dynamic variable that depends on several parameters related to structure, material, motions, and loading conditions etc. The combined characteristics of a TENG require solving a multi-parameter problem simultaneously so as to simulate the output performance. For this reason, a dimensionless approach, as presented here, is useful.

4. CONCLUSIONS

In summary, a systematic analysis of the generation of displacement current by use of a 3D mathematical model is provided for the linear sliding mote TENG, based on which a theoretical model to characteristic the basic AC output performances was developed. Firstly, our results shed light on the change of electric field and the generation of displacement current in TENGs, which are in opposite phase. Besides, for the first time, we find a bias voltage equivalent to a DC voltage contained in the basic AC output, giving rise to a big difference between a TENG and the traditional AC power generation system. In the light of our findings, the impedance of TENGs ($Z_T(t)$) is comprised by a DC component and several AC frequency components; and the rms value of $1/\omega C$ can be regarded as the optimum resistance of TENGs at steady state. Using a simple approach, we have demonstrated how optimization of the load resistance results in a substantially higher average power (77.5%) than the previously published method where the load resistance is optimized from the relaxation state alone. Furthermore, analytical equations of relaxation time and minimum needed

cycles are presented, describing the basic outputs of TENGs in the relaxation state. Finally, a normalization of the governing equation is derived using dimensional analysis, based on which the structural figure-of-merit of TENGs is expanded to cover steady state operation. It is predicted that a comprehensive understanding of the generation and variation of the displacement current from classical electrodynamics and the analytical methods of AC output theory that we use in this work can be utilized to also characterize other types of TENGs.

SUPPLEMENTARY MATERIAL

See the supplementary material for further details on the methods such as the FEM simulation, formula derivation and so on.

ACKNOWLEDGEMENTS

Research supported by the National Key R & D Project from Minister of Science and Technology (2016YFA0202704), National Natural Science Foundation of China (Grant No. 51432005 and 51702018), and China Postdoctoral Science Foundation (2019M660766).

REFERENCES

- ¹ United Nations Framework Convention on Climate Change (UNFCCC). Report of the Conference of the Parties on its Fifteenth Session, held in Copenhagen from 7 to 19 December 2009. Part Two: Action taken by the Conference of the Parties at its Fifteenth Session.
- ² M. Meinshausen, N. Meinshausen, W. Hare, S. C. B. Raper, K. Frieler, R. Knutti, D. J. Frame, M. R. Allen, Greenhouse-gas emission targets for limiting global warming to 2 °C, *Nature* **458**, 1158 (2009).
- ³ C. McGlade, P. Ekins, The geographical distribution of fossil fuels unused when limiting global warming to 2 °C, *Nature* **517**, 187 (2015).
- ⁴ J. Hansen, M. Sato, P. Kharecha, D. Beerling, R. Berner, V. Masson-Delmotte, M. Pagani, M. Raymo, D. L. Royer, J. C. Zachos, Target atmospheric CO₂: where should humanity aim? *Open Atmos. Sci. J* **2**, 217 (2008).
- ⁵ BP Statistical Review of World Energy (BP, 2019).
- ⁶ J. Rockström, O. Gaffney, J. Rogelj, M. Meinshausen, N. Nakicenovic, H. J. Schellnhuber.

This is the author's peer reviewed, accepted manuscript. However, the online version of record will be different from this version once it has been copyedited and typeset.

PLEASE CITE THIS ARTICLE AS DOI: 10.1063/1.5133023

- A roadmap for rapid decarbonization. *Science* **355**, 1269 (2017).
- ⁷ Z. L. Wang, On Maxwell's displacement current for energy and sensors: the origin of nanogenerators, *Mater. Today* **20**, 74 (2017).
- ⁸ C. Wu, A. C. Wang, W. Ding, H. Guo, Z. L. Wang, *Adv. Energy Mater* **9**, 1802906 (2019).
- ⁹ J. J. Shao, M. Willatzen, Y. Shi, Z. L. Wang, 3D mathematical model of contact-separation and single-electrode mode triboelectric nanogenerators, *Nano Energy* **60**, 630 (2019).
- ¹⁰ J. J. Shao, T. Jiang, W. Tang, X. Chen, L. Xu, Z. L. Wang, Structural figure-of-merits of triboelectric nanogenerators at powering loads, *Nano Energy* **51**, 688 (2018).
- ¹¹ J. J. Shao, M. Willatzen, T. Jiang, W. Tang, X. Chen, J. Wang, Z. L. Wang, Quantifying the power output and structural figure-of-merits of triboelectric nanogenerators in a charging system starting from the Maxwell's displacement current, *Nano Energy* **59**, 380 (2019).
- ¹² J. J. Shao, T. Jiang, W. Tang, L. Xu, T.W. Kim, C. Wu, X. Chen, B. Chen, T. Xiao, Y. Bai, Z. L. Wang, Studying about applied force and the output performance of slidingmode triboelectric nanogenerators, *Nano Energy* **48**, 292 (2018).
- ¹³ R. D. I. G. Dharmasena, K. D. G. I. Jayawardena, C. A. Mills, J. H. B. Deane, J. V. Anguita, R. A. Dorey, S. R. P. Silva, Triboelectric nanogenerators: providing a fundamental framework, *Energ. Environ. Sci.* **10**, 1801 (2017).
- ¹⁴ R. D. I. G. Dharmasena, K. D. G. I. Jayawardena, C. A. Mills, R. A. Dorey, S. R. P. Silva, A unified theoretical model for triboelectric nanogenerators, *Nano Energy* **48**, 391 (2018).
- ¹⁵ Y. Zi, S. Niu, J. Wang, Z. Wen, W. Tang, Z. L. Wang, Standards and figure-of-merits for quantifying the performance of triboelectric nanogenerators, *Nat. Commun.* **6**, 8376 (2015).
- ¹⁶ Y. Zi, J. Wang, S. Wang, S. Li, Z. Wen, H. Guo and Z. L. Wang, Effective energy storage from a triboelectric nanogenerator, *Nat. Commun.* **7**, 10987 (2016).
- ¹⁷ S. M. Niu, S. H. Wang, L. Lin, Y. Liu, Y. S. Zhou, Y. F. Hu, Z. L. Wang, Theoretical study of contact-mode triboelectric nanogenerators as an effective power source, *Energ. Environ. Sci.* **6**, 3576 (2013).
- ¹⁸ S. Niu, Z. L. Wang, Theoretical systems of triboelectric nanogenerators, *Nano Energy* **14**, 161 (2015).
- ¹⁹ S. Niu, Y. Liu, S. Wang, L. Lin, Y.S. Zhou, Y. Hu, Z. L. Wang, Theory of sliding-mode triboelectric nanogenerators, *Adv. Mater.* **25**, 6184 (2013).
- ²⁰ R. Hinchet, A. Ghaffarinejad, Y. Lu, J. Y. Hasani, S. W. Kim, P. Basset, Understanding and modeling of triboelectric-electret nanogenerator, *Nano Energy* **47**, 401 (2018).

This is the author's peer reviewed, accepted manuscript. However, the online version of record will be different from this version once it has been copyedited and typeset.

PLEASE CITE THIS ARTICLE AS DOI: 10.1063/1.5133023

- ²¹ H. Zhang, S. Feng, D. He, P. Molinié, J. Bai, Amplitude-variable output characteristics of triboelectric-electret nanogenerators during multiple working cycles, *Nano Energy* **63**, 103856 (2019).
- ²² M. Lu, W. Yin, A. Peyton, Z. Qu, X. Meng, Y. Xie, P. Zhao, J. Luo, Q. Zhao, Y. Tao, T. Zhou, Z. Zhang, A model for the triboelectric nanogenerator with inductive load and its energy boost potential, *Nano Energy* **63**, 103883 (2019).
- ²³ H. Qin, G. Cheng, Y. Zi, G. Gu, B. Zhang, W. Shang, F. Yang, J. Yang, Z. Du, Z. L. Wang, High energy storage efficiency triboelectric nanogenerators with unidirectional switches and passive power management circuits, *Adv. Funct. Mater.* **51**, 28 (2018).
- ²⁴ S. Xu, W. Ding, H. Guo, X. Wang, Z. L. Wang, Boost the performance of triboelectric nanogenerators through circuit oscillation, *Adv. Energy Mater.* **30**, 1900772 (2019).
- ²⁵ H. Zhang, L. Quan, J. Chen, C. Xu, C. Zhang, S. Dong, C. Lü, J. Luo, A general optimization approach for contact-separation triboelectric nanogenerator, *Nano Energy* **56**, 700 (2019).
- ²⁶ H. Zhang, C. Zhang, J. Zhang, L. Quan, H. Huang, J. Jiang, S. Dong, J. Luo, A theoretical approach for optimizing sliding-mode triboelectric nanogenerator based on multi-parameter analysis, *Nano Energy* **61**, 442 (2019).
- ²⁷ R. Hinchet, H. J. Yoon, H. Ryu, M. K. Kim, E. K. Choi, D. S. Kim, S. W. Kim, Transcutaneous ultrasound energy harvesting using capacitive triboelectric technology, *Science* **365**, 491 (2019).
- ²⁸ J. Chung, D. Heo, G. Shin, D. Choi, K. Choi, D. Kim, S. Lee, Ion-enhanced field emission triboelectric nanogenerator, *Adv. Energy Mater.* **9**, 1901731 (2019).
- ²⁹ J. Peng, S. D. Kang, G. J. Snyder, Optimization principles and the figure of merit for triboelectric generators, *Sci. Adv.* **3**, eaap8576 (2017).
- ³⁰ R. L. Boylestad, *Introductory circuit analysis*, 11th ed. Prentice Hall, Upper Saddle River, NY, USA, 2003.
- ³¹ C. K. Alexander, M. N. O. Sadiku, *Fundamentals of electric circuits*, McGraw-Hill Education, 2 Penn Plaza, NY, USA, 2017.
- ³² S. Niu, Y.S. Zhou, S. Wang, Y. Liu, L. Lin, Y. Bando, Z. L. Wang, Simulation method for optimizing the performance of an integrated triboelectric nanogenerator energy harvesting system, *Nano Energy* **8**, 150 (2014).

This is the author's peer reviewed, accepted manuscript. However, the online version of record will be different from this version once it has been copyedited and typeset.

PLEASE CITE THIS ARTICLE AS DOI: 10.1063/1.5133023

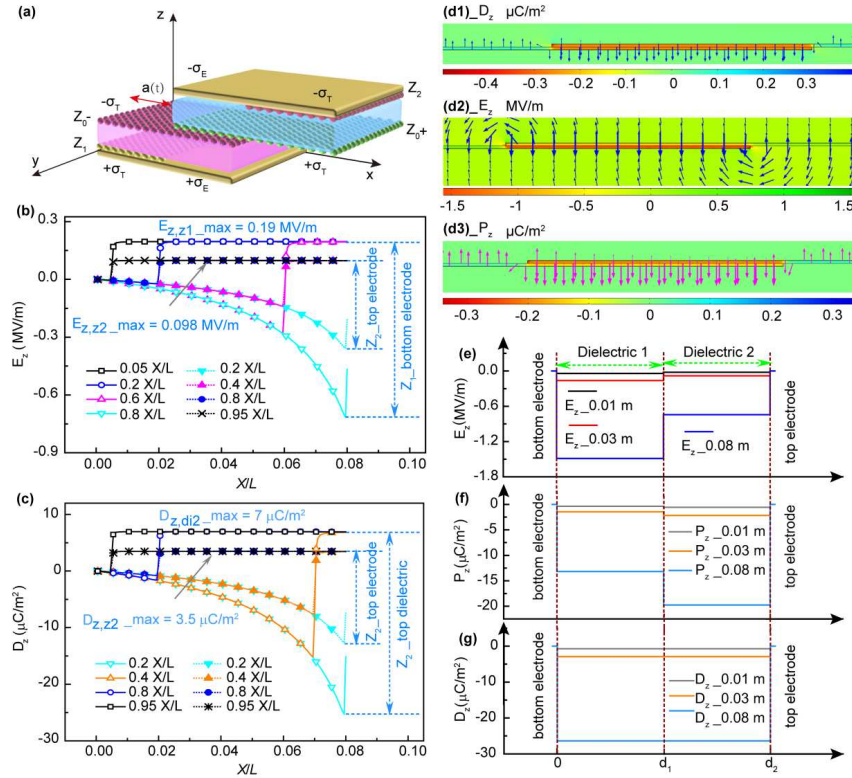


FIG. 1. Finite element modeling (FEM) simulation of a typical linear sliding (LS) mode triboelectric nanogenerator (TENG) at open-circuit (OC) conditions. (a) Schematic of a typical dielectric-to-dielectric LS mode TENG in Cartesian coordinates. (b, c) Calculated the z -component of (b) the electric field (E_z) distribution and (c) the electric displacement (D_z) distribution. z_1 and z_2 represent the positions of the top electrode-dielectric interface and bottom electrode-dielectric interface, respectively. (d1, d2 and d3) Distribution of the z -component of (d1) the electric displacement, (d2) the electric field and (d3) the polarization vector (P_z). (e, f, g). E_z (e), P_z (f), and D_z (g) inside the dielectric for the overlapping area change with the relative movement of the two triboelectric surfaces. Note that positions in the top electrode-dielectric interface (z_2) are specified relative to the positions in the bottom electrode-dielectric interface (z_1).

This is the author's peer reviewed, accepted manuscript. However, the online version of record will be different from this version once it has been copyedited and typeset.

PLEASE CITE THIS ARTICLE AS DOI: 10.1063/1.5133023

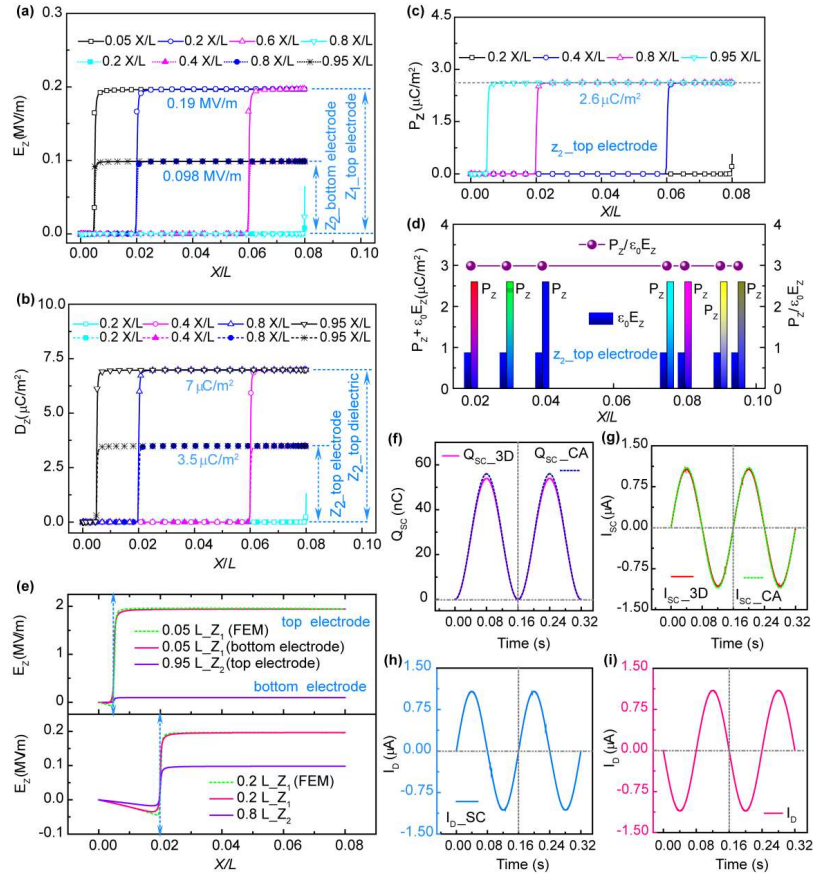


FIG. 2. FEM simulations and 3D model results of the LS mode TENG at short-circuit (SC) condition. (a, b, c) Calculation of the z-component of (a) the electric field (E_z) distribution, (b) the electric displacement (D_z) distribution, and (c) the polarization vector (P_z) distribution. (d) Relationship between $\epsilon_0 E_z$ and P_z at the z_2 position. Note that positions in the top electrode-dielectric interface (z_2) are specified relative to the positions in the bottom electrode-dielectric interface (z_1). (e) Comparison of E_z for relative separation distances based on FEM simulations and 3D mathematical model. (f, g) Comparison of the transferred charges (f) and short circuit current (g) using the 3D mode and the capacitance (CA) mode. (h, i) Variation of the displacement current (I_b) at (h) SC condition and (i) OC condition.

This is the author's peer reviewed, accepted manuscript. However, the online version of record will be different from this version once it has been copyedited and typeset.

PLEASE CITE THIS ARTICLE AS DOI: 10.1063/1.5133023

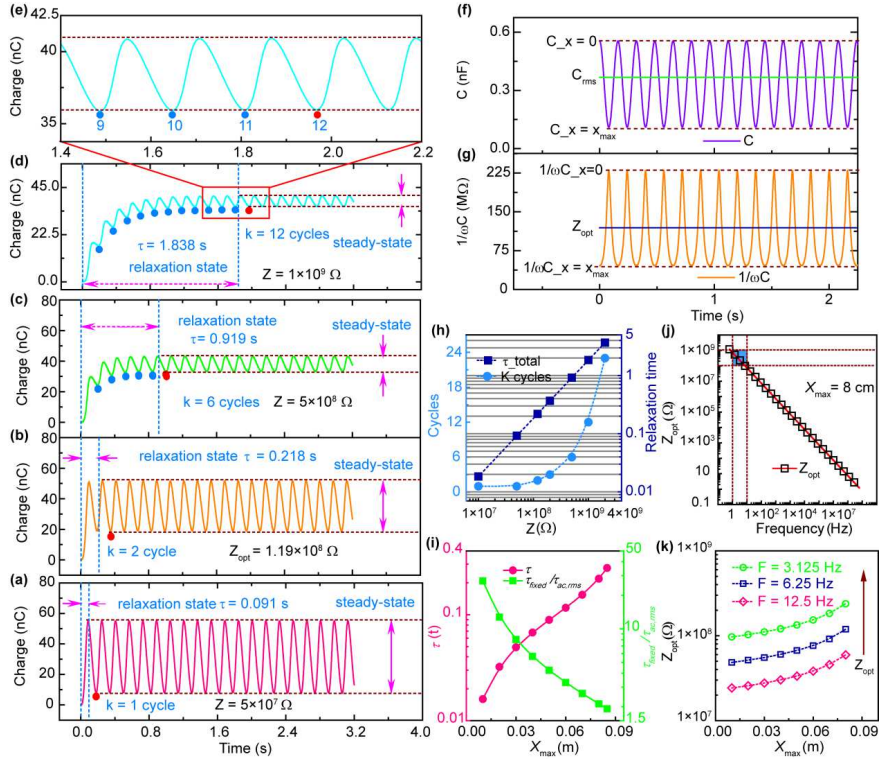


FIG. 3. AC output characteristics of the LS mode TENG and the optimum resistance in steady state. (a, b, c and d) Transferred charge vs. time for different loading conditions: (a) $Z = 5 \times 10^7 \Omega$, (b) $Z = Z_{\text{opt}}$, (c) $Z = 5 \times 10^8 \Omega$, (d) $Z = 1 \times 10^9 \Omega$. Two different states *i.e.*, the relaxation state and steady state can be seen in the cycles. (e) Local enlarged plots from fig. 3d to indicate the variation of the transferred charge from the relaxation state to steady state at $Z = 1 \times 10^9 \Omega$. (f) Capacitance of the LS mode TENG vs. time subject to periodic mechanical motion. Root-mean-square capacitance (C_{rms}) calculated from the periodic curve. (g) Reactance ($1/(\omega C)$) of the LS mode TENG vs. time for periodic mechanical motion. The root-mean-square reactance can be regarded as the optimum resistance (Z_{opt}) of the LS mode TENG at steady state. (h) Relaxation time (τ) and corresponding maximum needed cycles (k) for different load resistors. (i) The influence of the maximum separation distance (x_{max}) on the relaxation time and the ratio of $\tau_{\text{fixed}}/\tau_{\text{ac.rms}}$. τ_{fixed} and $\tau_{\text{ac.rms}}$ represent the relaxation time due to the fixed capacitance and time-varying capacitance of the LS mode TENG at different x_{max} , respectively. (j) Relationship between frequency and Z_{opt} . (k) Relationship between frequency and Z_{opt} for various x_{max} values.

This is the author's peer reviewed, accepted manuscript. However, the online version of record will be different from this version once it has been copyedited and typeset.

PLEASE CITE THIS ARTICLE AS DOI: 10.1063/1.5133023

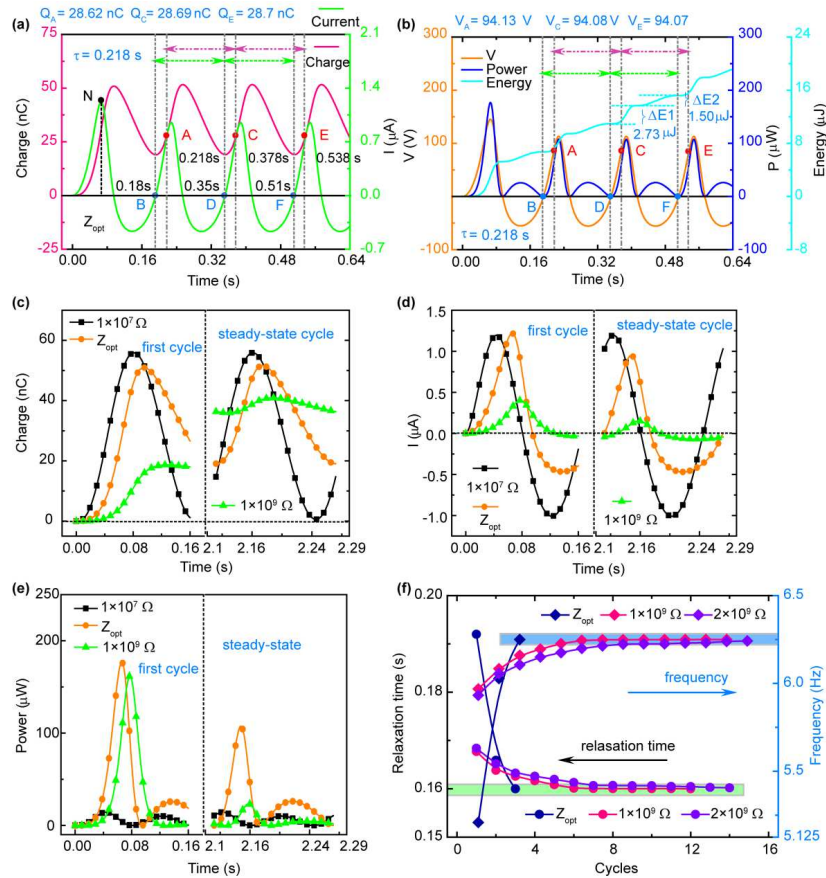


FIG. 4. AC output characteristics of the LS mode TENG and phase relations for different load resistances. (a) Transferred charges and current vs. time at $Z = Z_{\text{opt}} \Omega$. (b) Voltage, power and energy vs. time at $Z = Z_{\text{opt}} \Omega$. (c, d, e) Variations of the phase ((c) charge, (d) current, and (e) instantaneous power) from the first cycle to a steady state cycle for different load resistances. (f) Variations of the relaxation time and corresponding frequency for three typical load resistances.

This is the author's peer reviewed, accepted manuscript. However, the online version of record will be different from this version once it has been copyedited and typeset.

PLEASE CITE THIS ARTICLE AS DOI: 10.1063/1.5133023

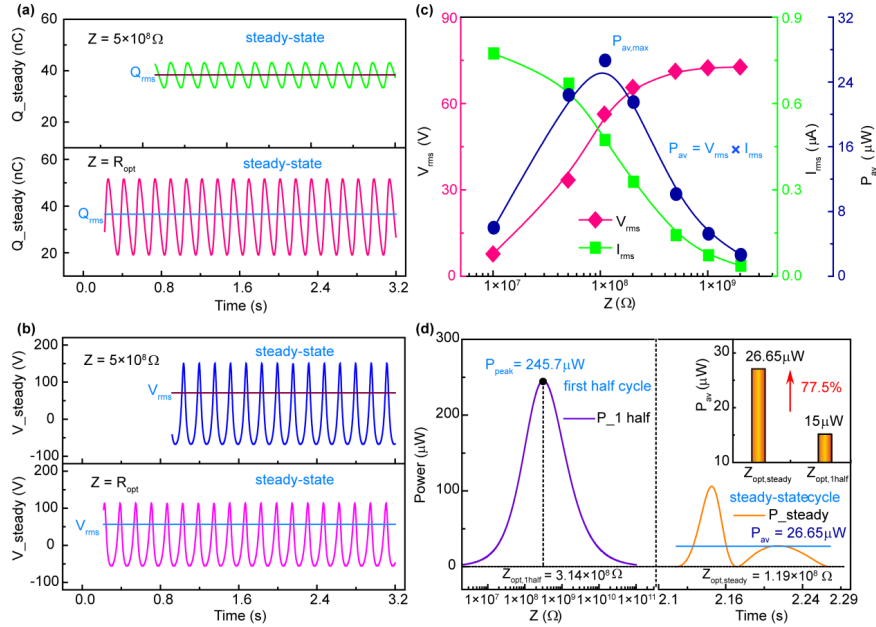


FIG. 5. AC output characteristics at steady state and root mean square values. (a, b) Comparisons of (a) charge-time and (b) voltage-time at load resistances of $Z = Z_{\text{opt}}$ and $Z = 5 \times 10^8 \Omega$, respectively. Observe that the root mean square represents the equivalent DC value of the signals at steady state. For instance, V_{rms} stands for the equivalent DC value or effective value of the voltage signal at steady state. (c) The influence of the load resistance on the equivalent DC value of the voltage (V_{rms}), current (I_{rms}) and average power (P_{ave}). Notice that P_{ave} is equal to the product of V_{rms} and I_{rms} , and the maximum average power ($P_{\text{ave,max}}$) can be obtained at Z_{opt} . (d) Comparison of the maximum average power from two different optimum resistances: the first one is from steady state ($Z_{\text{opt,steady}}$), and the other is for the first half cycle ($Z_{\text{opt,1half}}$) calculated using the same method as before. It can be clearly seen that the $P_{\text{ave,max}}$ at $Z_{\text{opt,steady}}$ is improved about 77.5% in comparison with that of $Z_{\text{opt,1half}}$.

This is the author's peer reviewed, accepted manuscript. However, the online version of record will be different from this version once it has been copyedited and typeset.

PLEASE CITE THIS ARTICLE AS DOI: 10.1063/1.5133023

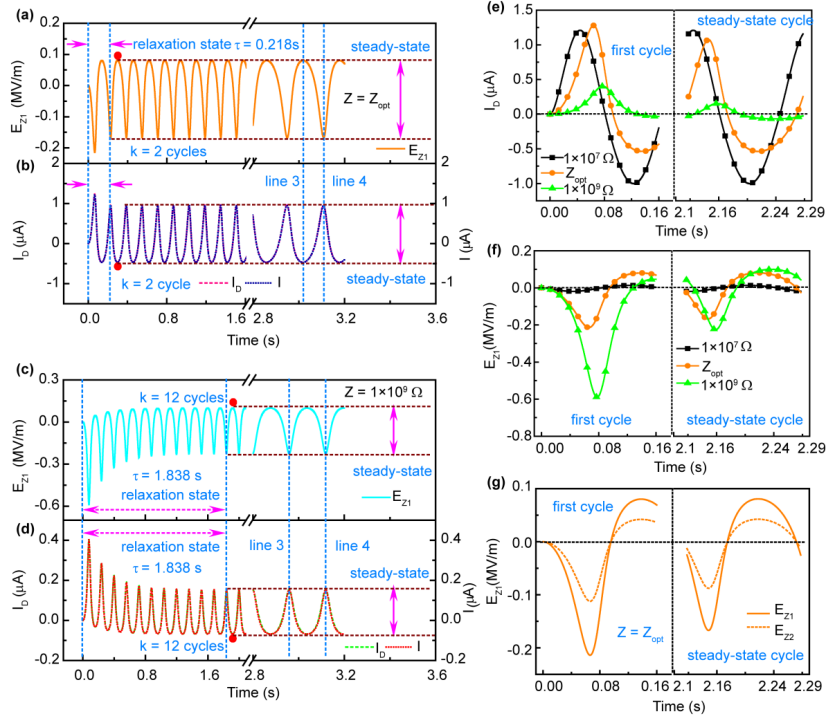


FIG. 6. Electric field and corresponding displacement current vs. time for different loading resistances. (a) Variation of electric field at the z_1 position (bottom electrode) and the corresponding (b) displacement current vs. time under the optimum resistance. (c) Variation of electric field at position z_1 and the corresponding (d) displacement current vs. time for a large resistor $Z = 1 \times 10^9 \Omega$. (e, f) Variations of the (e) displacement current and (f) electric field at position z_1 from the first cycle to a steady state cycle for different load resistances. (g) Comparison of the electric field at z_1 and z_2 positions from the first cycle to a steady state cycle at the optimum resistance.

This is the author's peer reviewed, accepted manuscript. However, the online version of record will be different from this version once it has been copyedited and typeset.
 PLEASE CITE THIS ARTICLE AS DOI: 10.1063/1.5133023

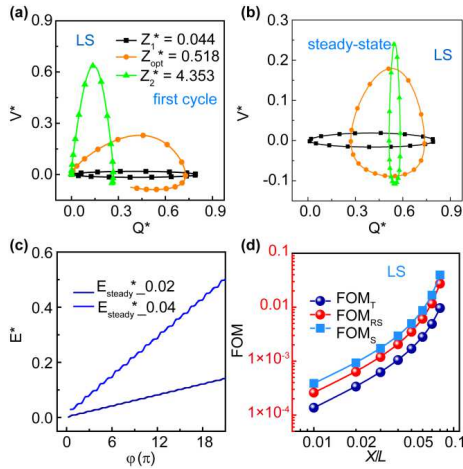
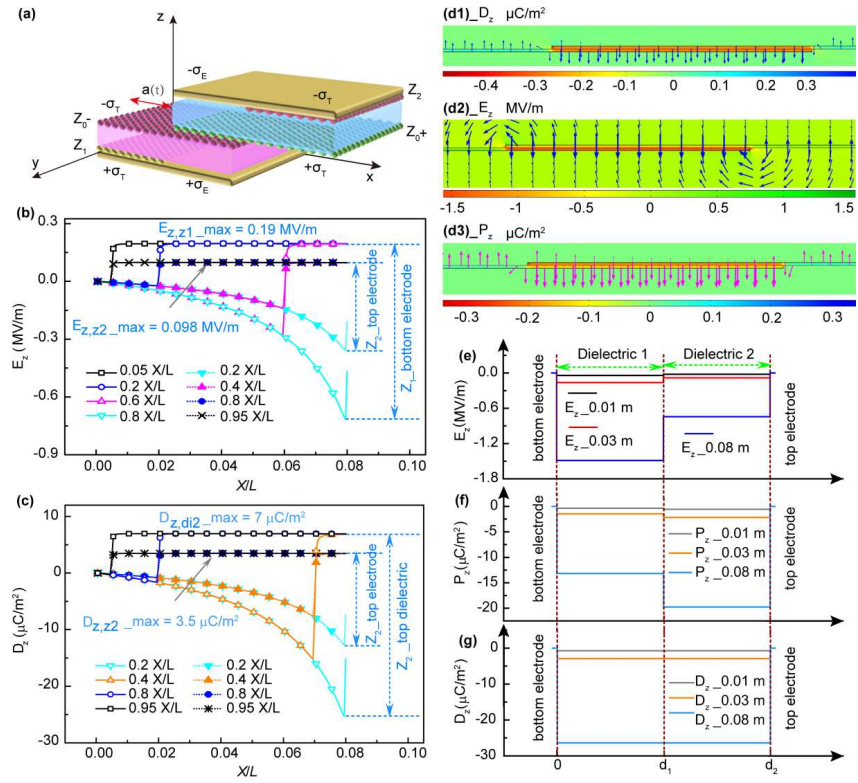


FIG. 7. Dimensionless analysis of the alternating current output performances of the LS mode TENG. (a, b) Q^*V^* diagrams from the first cycle to a steady state cycle for different Z^* . (c) Comparison of the E_{steady}^* at steady state for different x_{max}^* . (d) The figure-of-merits calculated in steady state (FOM_T) for the LS mode TENG. Note that FOM_{RS} and FOM_S represent the structural figure-of-merits of TENGs for Z_{opt} and infinite resistor, refer to Shao *et al.* (Ref. 10) and Zi *et al.* (Ref. 15), respectively.

This is the author's peer reviewed, accepted manuscript. However, the online version of record will be different from this version once it has been copyedited and typeset.

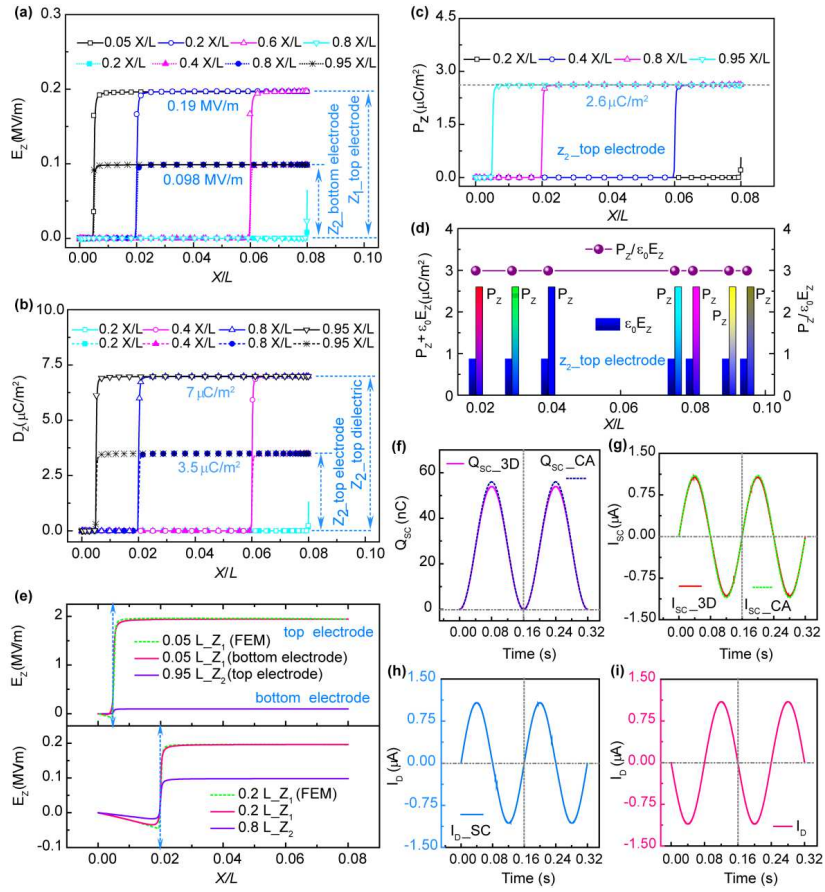
PLEASE CITE THIS ARTICLE AS DOI: 10.1063/1.5133023

FIG. 1.



This is the author's peer reviewed, accepted manuscript. However, the online version of record will be different from this version once it has been copyedited and typeset.
PLEASE CITE THIS ARTICLE AS DOI: 10.1063/1.5133023

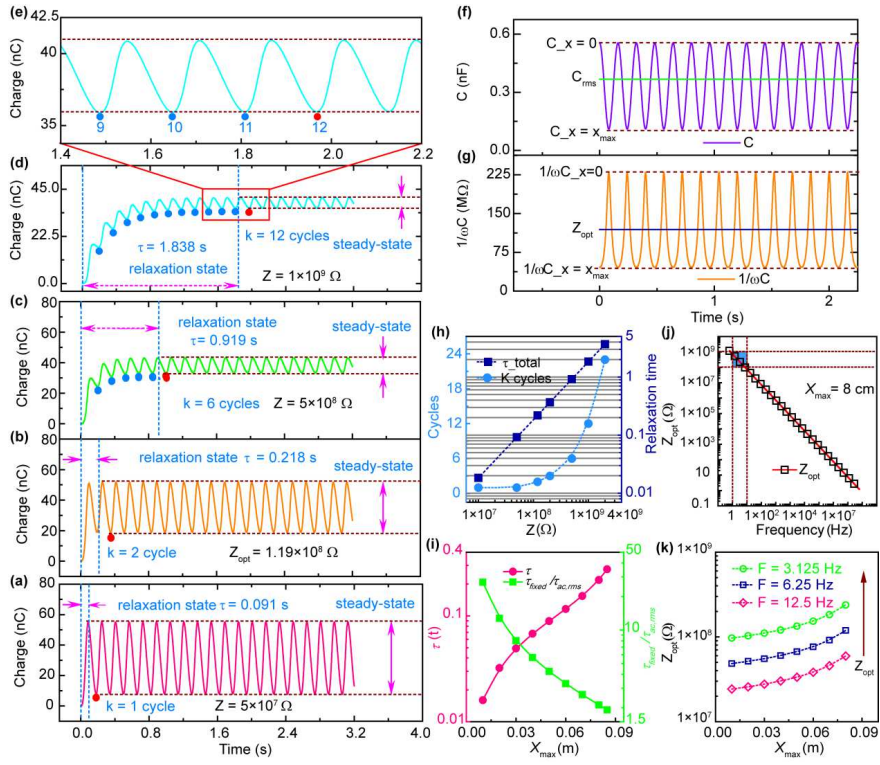
FIG. 2.



This is the author's peer reviewed, accepted manuscript. However, the online version of record will be different from this version once it has been copyedited and typeset.

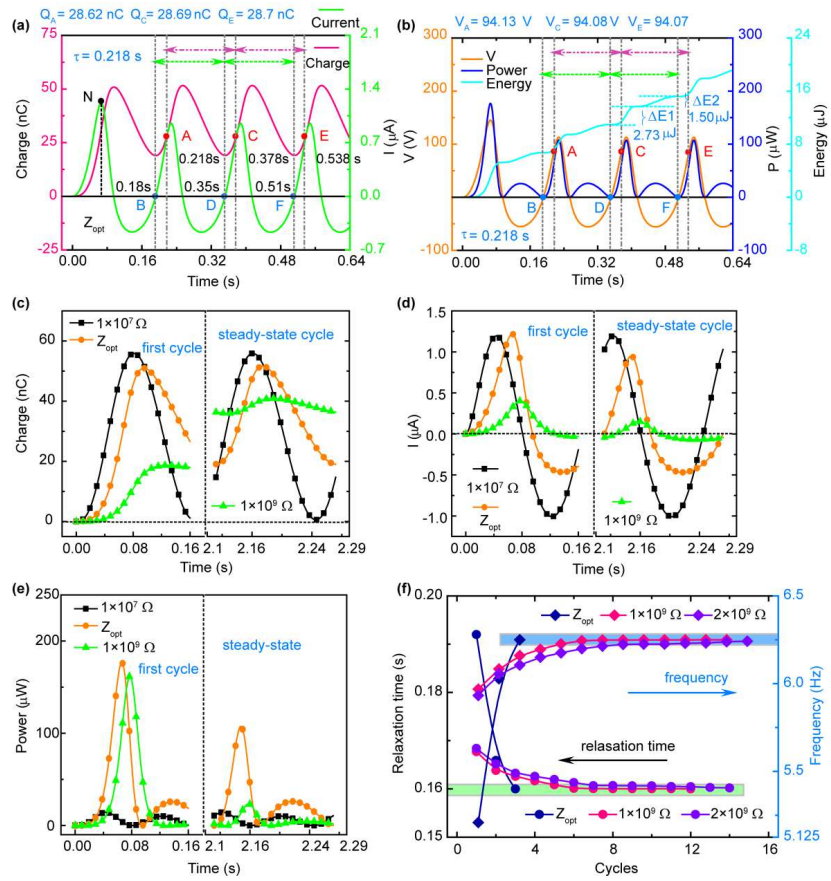
PLEASE CITE THIS ARTICLE AS DOI: 10.1063/1.5133023

FIG. 3.



This is the author's peer reviewed, accepted manuscript. However, the online version of record will be different from this version once it has been copyedited and typeset.
 PLEASE CITE THIS ARTICLE AS DOI: 10.1063/1.5133023

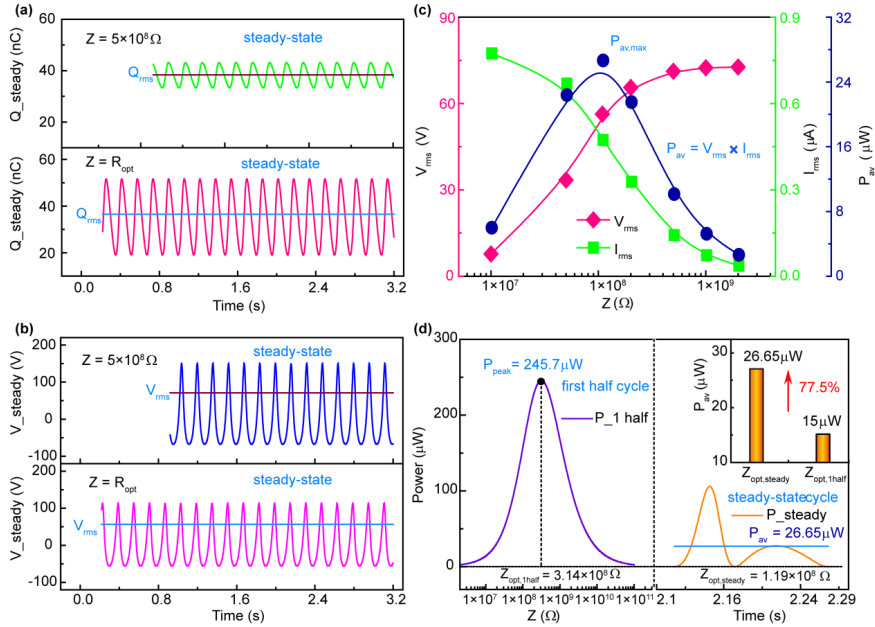
FIG. 4.



This is the author's peer reviewed, accepted manuscript. However, the online version of record will be different from this version once it has been copyedited and typeset.

PLEASE CITE THIS ARTICLE AS DOI: 10.1063/1.5133023

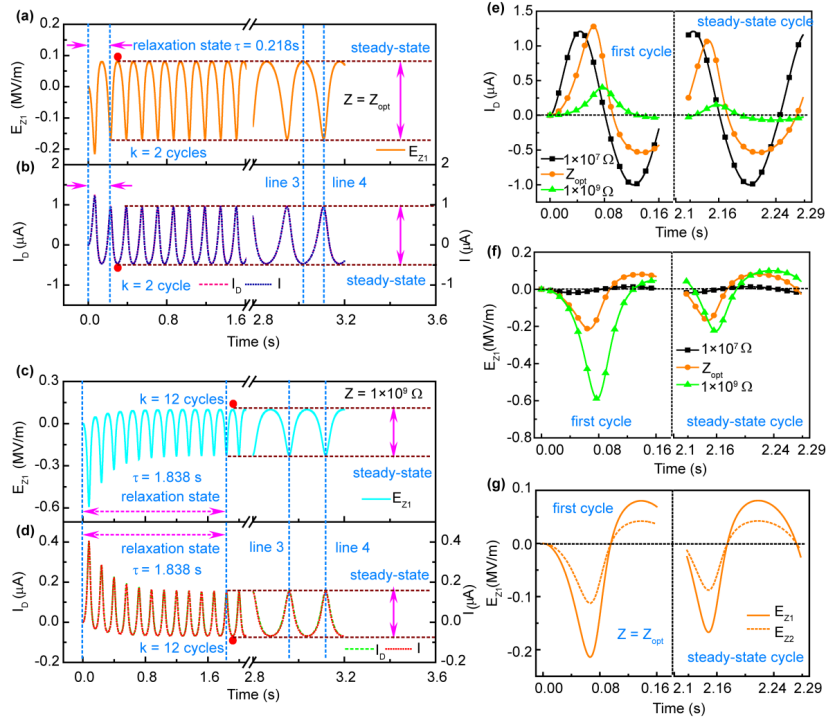
FIG. 5.



This is the author's peer reviewed, accepted manuscript. However, the online version of record will be different from this version once it has been copyedited and typeset.

PLEASE CITE THIS ARTICLE AS DOI: 10.1063/1.5133023

FIG. 6.



This is the author's peer reviewed, accepted manuscript. However, the online version of record will be different from this version once it has been copyedited and typeset.
 PLEASE CITE THIS ARTICLE AS DOI: 10.1063/1.5133023

FIG. 7.

